

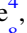






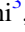

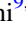
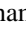

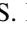


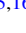

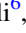
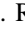
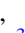



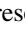
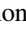


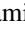
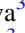

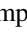
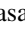

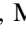


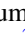



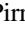




VADER: Probing the Dark Side of Dimorphos with LICIACube LUKE

Angelo Zinzi^{1,2} , P. H. A. Hasselmann³ , V. Della Corte⁴ , J. D. P. Deshapriya³ , I. Gai⁵ , A. Lucchetti⁶ , M. Pajola⁶ ,
 A. Rossi⁷ , E. Dotto³ , E. Mazzotta Epifani³ , R. T. Daly⁸ , M. Hirabayashi^{9,10} , T. Farnham¹¹ , C. M. Ernst⁸ ,
 S. L. Ivanovski¹² , J.-Y. Li¹³ , L. M. Parro^{14,15,16} , M. Amoroso¹ , J. Beccarelli⁶ , I. Bertini¹⁷ , J. R. Brucato¹⁸ ,
 A. Capannolo¹⁹ , S. Caporali¹⁸ , M. Ceresoli²⁰ , G. Cremonese⁶ , M. Dall’Ora⁴ , L. Gomez Casajus⁵ , E. Gramigna⁵ , S. Ieva³ ,
 G. Impresario¹ , R. Lasagni Manghi⁵ , M. Lavagna²⁰ , M. Lombardo⁵ , D. Modenini⁵ , B. Negri¹ , P. Palumbo²¹ , D. Perna³ ,
 S. Pirrotta¹ , G. Poggiali^{18,22} , P. Tortora⁵ , F. Tusberti⁶ , M. Zannoni⁵ , and G. Zanotti²⁰ 

¹ Agenzia Spaziale Italiana, Via del Politecnico, snc, 00133, Rome, Italy; angelo.zinzi@asi.it

² ASI—Space Science Data Center, Via del Politecnico, snc, 00133, Rome, Italy

³ INAF-Osservatorio Astronomico di Roma, Via Frascati, 33, 00078, Monte Porzio Catone, Roma, Italy

⁴ INAF-Osservatorio Astronomico di Capodimonte, Salita Moiarriello, 16, 80131 Napoli, Italy

⁵ Alma Mater Studiorum—Università di Bologna, Dipartimento di Ingegneria Industriale, Via Fontanelle, 40, 47121 Forlì, Italy

⁶ INAF-Astronomical Observatory of Padova, Vic. Osservatorio 5, 35122 Padova, Italy

⁷ IFAC-CNR, Via Madonna del Piano, 10, 50019, Sesto Fiorentino, Firenze, Italy

⁸ Johns Hopkins University Applied Physics Laboratory, 11100 Johns Hopkins Road, Laurel, MD 20723, USA

⁹ Daniel Guggenheim School of Aerospace Engineering, Georgia Institute of Technology, North Avenue, Atlanta, GA 30332, USA

¹⁰ Department of Aerospace Engineering, Auburn University, Davis Hall, 211 Aerospace Engineering Bldg, AL 36849, USA

¹¹ University of Maryland, College Park, MD 20742, USA

¹² INAF-Osservatorio Astronomico di Trieste, Via G.B. Tiepolo, 11, 34143, Trieste, Italy

¹³ Planetary Science Institute, 1700 E Fort Lowell Road STE 106, Tucson, AZ 85719, USA

¹⁴ IUFACyT, Universidad de Alicante, Carretera San Vicente del Raspeig s/n, 03690 Alicante, Spain

¹⁵ University of Arizona, 1200 E University Boulevard, Tucson, AZ 85721, USA

¹⁶ Universidad Complutense, Av. Complutense, s/n, Moncloa - Aravaca, 28040, Madrid, Spain

¹⁷ Università degli Studi di Napoli “Parthenope,” Dipartimento di Scienze & Tecnologie, Centro Direzionale, Isola C4, 80133, Napoli, Italy

¹⁸ INAF-Osservatorio Astrofisico di Arcetri, Largo Enrico Fermi, 5, 50125 Firenze, Italy

¹⁹ Institut Supérieur de l’Aéronautique et de l’Espace (ISAE-SUPAERO), Université de Toulouse, 10 Av. Edouard Belin, 31400, Toulouse, France

²⁰ Politecnico di Milano—Bovisa Campus, Dipartimento di Scienze e Tecnologie Aerospaziali Via Raffaele Lambruschini, 20156, Milano, Italy

²¹ INAF-Istituto di Astrofisica e Planetologia Spaziali, Via del Fosso del Cavaliere, 100, 00133, Roma, Italy

²² LESIA-Observatoire de Paris PSL, Section de Meudon 5, Place Jules Janssen 92195 MEUDON Cedex, France

Received 2023 December 21; revised 2024 March 13; accepted 2024 March 25; published 2024 April 25

Abstract

The ASI cubesat LICIACube has been part of the first planetary defense mission DART, having among its scopes to complement the DRACO images to better constrain the Dimorphos shape. LICIACube had two different cameras, LEIA and LUKE, and to accomplish its goal, it exploited the unique possibility of acquiring images of the Dimorphos hemisphere not seen by DART from a vantage point of view, in both time and space. This work is indeed aimed at constraining the tridimensional shape of Dimorphos, starting from both LUKE images of the nonimpacted hemisphere of Dimorphos and the results obtained by DART looking at the impacted hemisphere. To this aim, we developed a semiautomatic Computer Vision algorithm, named VADER, able to identify objects of interest on the basis of physical characteristics, subsequently used as input to retrieve the shape of the ellipse projected in the LUKE images analyzed. Thanks to this shape, we then extracted information about the Dimorphos ellipsoid by applying a series of quantitative geometric considerations. Although the solution space coming from this analysis includes the triaxial ellipsoid found by using DART images, we cannot discard the possibility that Dimorphos has a more elongated shape, more similar to what is expected from previous theories and observations. The result of our work seems therefore to emphasize the unique value of the LICIACube mission and its images, making even clearer the need of having different points of view to accurately define the shape of an asteroid.

Unified Astronomy Thesaurus concepts: Asteroids (72); Near-Earth objects (1092)

1. Introduction

The Light Italian Cubesat for Imaging of Asteroids (LICIACube; Dotto et al. 2021) was a 6U cubesat contributed by the Italian Space Agency (ASI—Agenzia Spaziale Italiana) that took part in the NASA DART mission (Rivkin et al. 2021) that impacted Dimorphos, the secondary of the Didymos binary asteroid system. LICIACube complemented DART observations and offered a unique and changing point of view at spatial

and temporal resolutions not allowed by other instruments during the very first minutes after the impact, which occurred on 2022 September 26, 23:14:24.183 UTC (Dotto & Zinzi 2023; Thomas et al. 2023).

One of the main objectives of LICIACube was to “obtain multiple images of Dimorphos showing the non-impacted hemisphere, hence increasing the accuracy of the shape and volume determination” (Dotto et al. 2021).

While the scope of the DART mission was to impact Dimorphos, the secondary of the 65803 Didymos binary system, LICIACube was designed to perform a flyby of Dimorphos (~150 m diameter) and Didymos (~730 m). The success of this kind of operation (Dotto et al. 2024) constituted



Original content from this work may be used under the terms of the [Creative Commons Attribution 4.0 licence](https://creativecommons.org/licenses/by/4.0/). Any further distribution of this work must maintain attribution to the author(s) and the title of the work, journal citation and DOI.

the first intentional flyby mission to a binary asteroid system (the NASA Galileo already flew past 243 Ida and Dactyl in 1993, but Dactyl was discovered during the same flyby and thus cannot be considered an intentionally planned flyby of a binary asteroid system as that of LICIACube is). During the LICIACube flyby, and enabled by its autonomous tracking capabilities, its two cameras, the panchromatic LICIACube Explorer Imaging for Asteroid (LEIA) and the RGB LICIACube Unit Key Explorer (LUKE), performed a series of image acquisitions at different distances from the target with different viewing geometries and exposure times.

In particular, beginning on 2022 September 26, 23:17:17.000 UTC, LICIACube started imaging Dimorphos's nonimpact hemisphere, the one not observed by DART, nor by any other instrument with spatial resolution comparable to that of the LICIACube cameras.

Even though only a fraction of Dimorphos was directly illuminated by the Sun from the LICIACube observing geometry, in the present study we analyze a combination of LUKE images with exposure times and viewing conditions that have allowed recovering its nightside hemisphere.

For such an analysis we developed a technique aimed at fulfilling the objective cited above using Computer Vision techniques. We named it the Visual Algorithm for Dimorphos Ellipsoid Recognition (VADER), allowing us to constrain the 3D shape of Dimorphos. This gives an independent and complementary benchmark for the results found by using only DART Didymos Reconnaissance and Asteroid Camera for OpNav (DRACO; Fletcher et al. 2022) images and described by Daly et al. (2023, 2024).

In this work we first describe the data set taken into consideration (Section 2), before providing an accurate description of the VADER algorithm and of the methods used here to constrain the shape of Dimorphos (Section 3), discussing our findings (Section 4), matching them with the state of the art (both theoretical and observational) about the shape of Dimorphos (Section 5), and wrapping it up with concluding remarks (Section 6).

2. Data Set Considered

The LUKE camera on board LICIACube is a dioptric camera composed of four refractive elements, with a diagonal field of view (FOV) of 10° , with a CMOS sensor (CMV2000) detector with 2048×1088 pixels at 10-bit depth (with an effective 8-bit depth for the raw images). Its detector is built using a Bayer pattern; therefore, by using a 2D sensor, it is able to detect multiple colors, without using any filter wheel. This is allowed by the location of red, green, and blue pixels throughout the detector following a predetermined scheme. The final RGB full resolution image is reconstructed by exploiting well-known and tested debayering algorithms (e.g., Menon et al. 2007).

In particular, the LUKE Bayer pattern scheme is the so-called "RGGB," in which for every 2 green pixels (G) are present 1 red (R) pixel and 1 blue (B) pixel.

We decided to use only the green plane for this study because it has been demonstrated to be the most reliable one, in both reconstruction of the scene (as the G pixels are twice as dense as the R and B) and radiance values (see the calibration document available on the LICIACube SOC).²³

Since no accurate information about the physical characteristics of Dimorphos and the plume has been available before the DART/LICIACube images, the LICIACube team decided to use a peculiarity of the LUKE camera in order to assure the best exploitation possible of the images.

In particular, images are acquired as "triplets," i.e., three swiftly acquired images, with different integration times, separated in time only by their exposure times and camera processing time.

The time interval between the first and the third image of the triplet was around 50 ms, and the three integration times (which in order are short, medium, and long) have been estimated on the basis of the known physical characteristics of the target, taking into consideration the distance between the target and LICIACube.

Both these values (image timing separation and integration times) can vary for every triplet, so that the team raised the probability of having at least one image with an adequate signal level for the surface and another one for the plume for every triplet.

Among the 120 images acquired by LUKE after the closest approach (CA), only four images have been used in this work: considering the uncertainties in both size and signal, they are indeed the only ones characterized by a combination of spatial resolution and viewing conditions pivotal to perform an analysis with adequate accuracy.

Figure 1 shows an example of how the nonilluminated part of Dimorphos is viewed in contrast to the saturated part of the image owing to the brightness caused by the illumination of the primary, Didymos, and the ejecta plume generated after the impact of DART.

3. Projected Ellipse and Actual Ellipsoid Retrieval

3.1. VADER

The algorithm used here, designed by the LICIACube team for this specific work and developed in Python using several functions of the OpenCV package,²⁴ is designed to find shapes of a desired size inside monochromatic images, working with thresholded images.

Albeit expressly developed for this application, VADER can be adapted to recognize objects in several types of images.

Here we look for objects of sizes between 3000 and 10,000 m², roughly corresponding to what is expected for half of the Dimorphos hemisphere, converting from physical units (i.e., radiance) images to thresholded ones, by selecting a radiance threshold.

Before applying this thresholding, we passed from physical radiance to its bit-scaled counterpart: this step allowed us to work with a finite value range (defined between 0 and 255, taking into account the original LUKE raw image bit depth) and eliminate the saturated pixels, which, from the standard $1e30$ value in the FITS files, have been set to NaN (Not a Number), readily excluded by the analysis.

Since the images considered have differences in exposure time, distance from the target, and illumination condition, we had to find a threshold value specific for each image analyzed. We made this by applying a semiautomatic thresholding function able to detect the object inside the expected shape range around the desired position range inside the LUKE FOV.

²³ https://www.ssdsc.asi.it/liciacube/archive/data/document/asi_liciacube_leialuke_calibration_pipeline_description.pdf

²⁴ <https://pypi.org/project/opencv-python/>



Figure 1. Zoom-in of the liciacube_luke_i2_1664234241_00417_01 green channel image showing the nightside hemisphere of Dimorphos after the impact (highlighted by the red circle).

The thresholding level has been automatically selected by the function between several steps from 220 to 45: in the first step the function finds an object of the indicated size in the expected area of the image (this one is provided by the user, changing from image to image in a nondetermined way, due to the complex attitude of the spacecraft during the flyby). Subsequently, the geometric information about the object is stored, such as (a) the centroid, (b) the rotation angle, (c) the size of the rectangle in which the object (the Dimorphos dark hemisphere identified) is inscribed (Figure 2), and (d) the area of the selected object.

For this specific work, we applied VADER to extract the part of Dimorphos not directly illuminated by the Sun (i.e., the nightside hemisphere, highlighted by the red contour in Figure 2), which is the input needed to start the next step of the algorithm, devoted to extracting the projected ellipses defining the shape of Dimorphos.

3.2. Projected Ellipse Reconstruction

By retrieving the semiminor axis b of this projected ellipse and the fraction of the illuminated part of Dimorphos from images and determining the sub-spacecraft latitude and longitude together with the area of the nightside part of the ellipse from known observational geometries, it is possible to compute the corresponding semimajor axis a (Figure 2) by inverting the formula for the ellipse area

$$a = A/(\pi xb), \quad (1)$$

where a is the semimajor axis, b is the semiminor axis, and A is the ellipse area.

To this aim, the longer side of the rectangle found by VADER is considered to correspond to the entire (not semi-) minor axis of the ellipse viewed by LUKE representing Dimorphos; the shorter side is considered to be a part of the major axis of the ellipse (Figure 2).

This part would exactly correspond to the semimajor axis if the ellipse would have been half illuminated. However, since observational geometries are not defined to be these ones, we used simulated images, computed from NAIF SPICE kernels (Acton 1996; Acton et al. 2017), to retrieve the percentage of

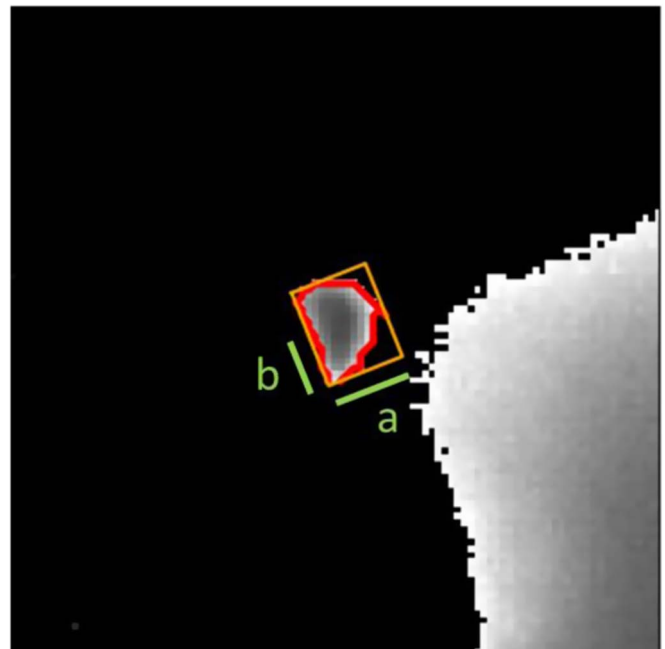


Figure 2. Example of the axes retrieval by VADER in a LUKE image (4241 one zoomed in—see Table 1 for definition of images). The orange rectangle is the one identified by VADER as the area in which the dark hemisphere is inscribed. The long axis “ a ” is as long as the rectangle side used to retrieve it, whereas the short axis “ b ” is half of the rectangle side used for its computation. Note that, with respect to Figure 1, the dark areas are those bright in Figure 1 (i.e., in the original LUKE image); this is due to the thresholding described in the text.

the illuminated part of the ellipse and, in turn, the total area of the ellipse (visible and not visible in the selected LUKE image) as

$$A = \text{DAF}/\text{DAFP}, \quad (2)$$

where A is the total area of the projected ellipse, DAF is the dark area found, DAFP is the dark area fraction predicted (using kernels of instrument, camera and Dimorphos), expressed in fraction of the unity.

Table 1
Subspacecraft Longitudes and Latitudes for the Analyzed Images

Image	Acquisition Time (UTC)	Exposure Time (s)	Pixel Size (m pixel ⁻¹)	Sub-S/C Longitude (deg)	Sub-S/C Latitude (deg)
4241	23:17:21.041	0.035	6.4	122.2	-28.7
4242	23:17:22.052	0.05	6.8	120.4	-26.4
4243	23:17:23.011	0.01	7.2	118.9	-24.3
4244	23:17:24.041	0.035	7.5	117.5	-22.3

Once the total area of the projected ellipse is also known, it can be used to finally compute the semimajor ellipse axis, by inverting the formula for the ellipse area.

3.3. Ellipsoid Computation

The following step, the reconstruction of the real 3D ellipsoid sizes starting from its ellipse projected in the FOV, is a nontrivial geometric problem, requiring several images, acquired from very different viewpoints to be well determined.

In our case, the relative positions of LICIACube and Dimorphos are not so different, as the time between the first and last available images was only 4 s.

This is evidenced by the subspacecraft points, which, expressed as latitude and longitude as retrieved by the NAIF SPICE kernels, differ by less than 10° (see Table 1).

Another approach able to provide information about the shape of the ellipsoid starting from the viewed ellipse, but not on its absolute axis sizes, is that described by Binggeli (1980). By indicating with β the apparent minor-to-major-axis ratio b/a , where p and q are the ratios between the three ellipsoid axes (i.e., $p = Y/X$ and $q = Z/X$), with Φ the subspacecraft longitude and with θ the subspacecraft latitude (this one ranging from 0° to 180°), he found

$$\beta(p, q, \phi, \theta) = \frac{\{j + l - [(j - l)^2 + 4k]^{1/2}\}}{\{j - l + [(j - l)^2 + 4k]^{1/2}\}} \quad (3a)$$

$$j(p, q, \phi, \theta) = q^2 \sin^2 \theta + p^2 \sin^2 \phi \times \cos^2 \theta + \cos^2 \phi \cos^2 \theta \quad (3b)$$

$$l(p, q, \phi, \theta) = p^2 \cos^2 \phi + \sin^2 \phi \quad (3c)$$

$$k(p, q, \phi, \theta) = (1 - p^2) \sin \phi \cos \phi + \cos \theta. \quad (3d)$$

To compute β , we analytically solved Equations (3b)–(3d) for p and q in the range [0, 1] with steps of 0.005 and then putting the j, l, k , values so computed in the formula given by Equation (3a). We indicated the results as valid only if comprised in a $\pm 20\%$ margin with respect to the a/b value found from the single image as retrieved by VADER.

This error consideration comes from the fact that the total intrinsic error of the RGG Bayer pattern for the G plane could be considered to be 3 pixels (i.e., the considered pixel ± 1 pixel), since for every “real” pixel there is a “virtually retrieved” 1 pixel.

In particular, by considering the Nyquist frequency and its comparison with a classical (i.e., non-Bayer) detector, we have that the spatial resolution of the green channel of a Bayer pattern detector is no worse than $\sqrt{2} * r$, where r is the resolution of the classical detector (Carlsson 2016).

In the images here analyzed, taking into consideration the distance between LICIACube and Dimorphos (known with an accuracy of 2 km at the CA) and the LUKE instantaneous FOV, the resolution is roughly 7 m pixel⁻¹ (varying from 6.5 to 7.4, as described in Table 1). Hence, the error can be considered to be ± 10 m.

This value, compared to the measurement of the Dimorphos projected ellipse minor axis, which is roughly 100 m, led the error to be considered as 10% of the measure, which was then applied to all the measurements and results in this work and, by error propagation, leads to the $\pm 20\%$ stated above for the axis ratio.

Once these values are known for each image, it is then possible to obtain a range of physically plausible values for the axis ratios of the Dimorphos ellipsoid.

4. Discussion

The four LUKE images selected (Figure 3) come from consecutive LUKE “triplets,” all acquired in the post-CA phase of LICIACube, with spatial resolution spanning from 6.4 to 7.5 m pixel⁻¹ and exposure times from 0.01 to 0.05 s (Table 1).

All the images have a similar dark area (i.e., the area of the object with pixel values larger than the applied threshold, DAF in Equation (2)) as retrieved by VADER, by taking into consideration the measurement errors (Table 2): this would have been expected considering the slight variation of illumination conditions.

In order to compute the expected night area fraction (DAFP in Equation (2)), a value needed to find the total area, we performed a preliminary analysis on the limit value for the incidence angle to consider the start of “nighttime” illumination conditions.

In order to apply the VADER algorithm to LUKE images of interest for this study, we decided to use a threshold for the incidence angle of 100°, even if, by definition, this computation should have been performed for the pixels with incidence angle larger than 90°, as this value defines the position of the terminator.

However, by selecting the “default” threshold, the subsequent computation returned a projected shape for Dimorphos much too similar to a circle (Figure 3, cyan contours). This is evident also by comparing the “Axis Ratio” column in Table 2, where the values with incidence angle threshold set to 90° are always consistent with 1 (i.e., close to axisymmetric), within the errors.

This too circular appearance of the projected shape is in disagreement with what is expected in a general case for the projection of an ellipsoid (as expected for the shape of a secondary asteroid such as Dimorphos; Pravec et al. 2016; Daly et al. 2023) on a plane (i.e., the FOV of LICIACube cameras) is defined as an ellipse. The shape expected in this case is an ellipse, and although a circle is a special type of an ellipse, it would require a very peculiar point of view from LICIACube to obtain a circle as a projection of the Dimorphos shape.

This discrepancy could be due to several factors, likely including the spatial resolution of the images and their associated uncertainties. Indeed, as at 7 m pixel⁻¹ the resolution in incidence angle roughly corresponds to 5° on the surface of Dimorphos, accounting for the 10% accuracy in size measurements broadly used in this work, the incidence angle threshold suffers from 9° of uncertainty.

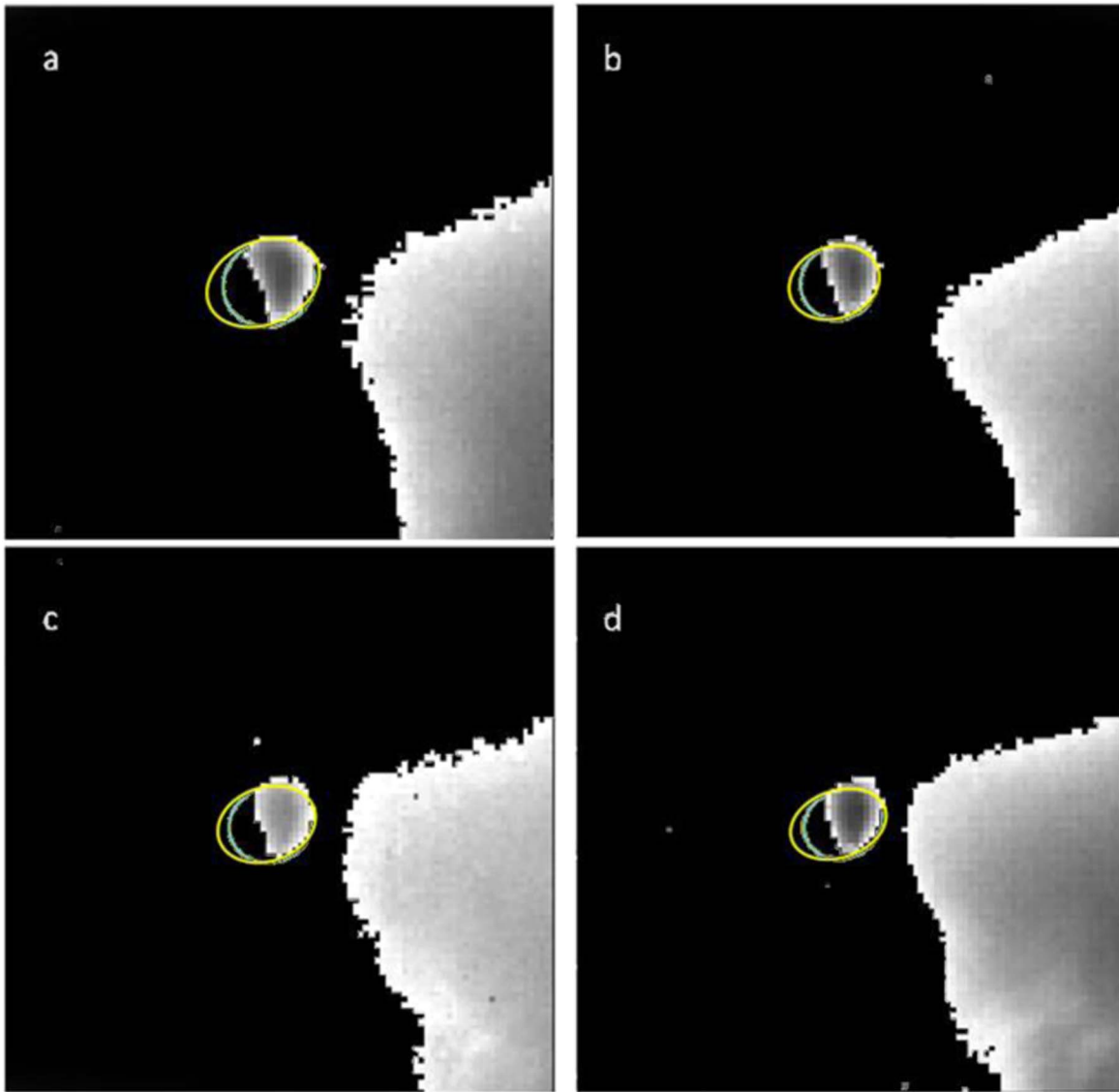


Figure 3. The four images selected, with the ellipses computed after the thresholding process by VADER. Cyan ellipses are computed with incidence angle threshold set at 90° ; yellow ones are computed using an incidence angle threshold set at 100° . (a) Image 4241; (b) image 4242; (c) image 4243; (d) image 4244 (see Table 1 for definitions of images).

Table 2
Computed and Extracted Values for the Ellipses Retrieved from the Four Images Selected at Two Different Incidence Angle Thresholds

Image	Incidence Threshold (deg)	Dark Area (m ²)	Night Fraction (%)	Total Computed Area (m ²)	Axis <i>a</i> (m)	Axis <i>b</i> (m)	Axis Ratio
4241	90	5100	60	8500	54	50	1.08
4242	90	4200	62	6700	47	45	1.04
4243	90	5200	62	8300	54	48	1.13
4244	90	5300	67	7900	54	46	1.17
4241	100	5100	47	11,000	69	50	1.38
4242	100	4200	51	8200	58	45	1.29
4243	100	5200	51	10,000	66	48	1.38
4244	100	5300	53	10,000	68	46	1.48

Note. The size measurement uncertainty is always 10% of the value, apart from the “Total Computed Area” and “Axis Ratio,” where the propagation of the error gives an error of 20%.

Applying the same reasoning, an incidence angle threshold fixed at 100° is compatible with the “classical” 90° considering a 10% uncertainty.

Using this 100° threshold value, we obtain results in line with the general case in which the projection should have been an ellipse. This is also confirmed by the values in the “Axis

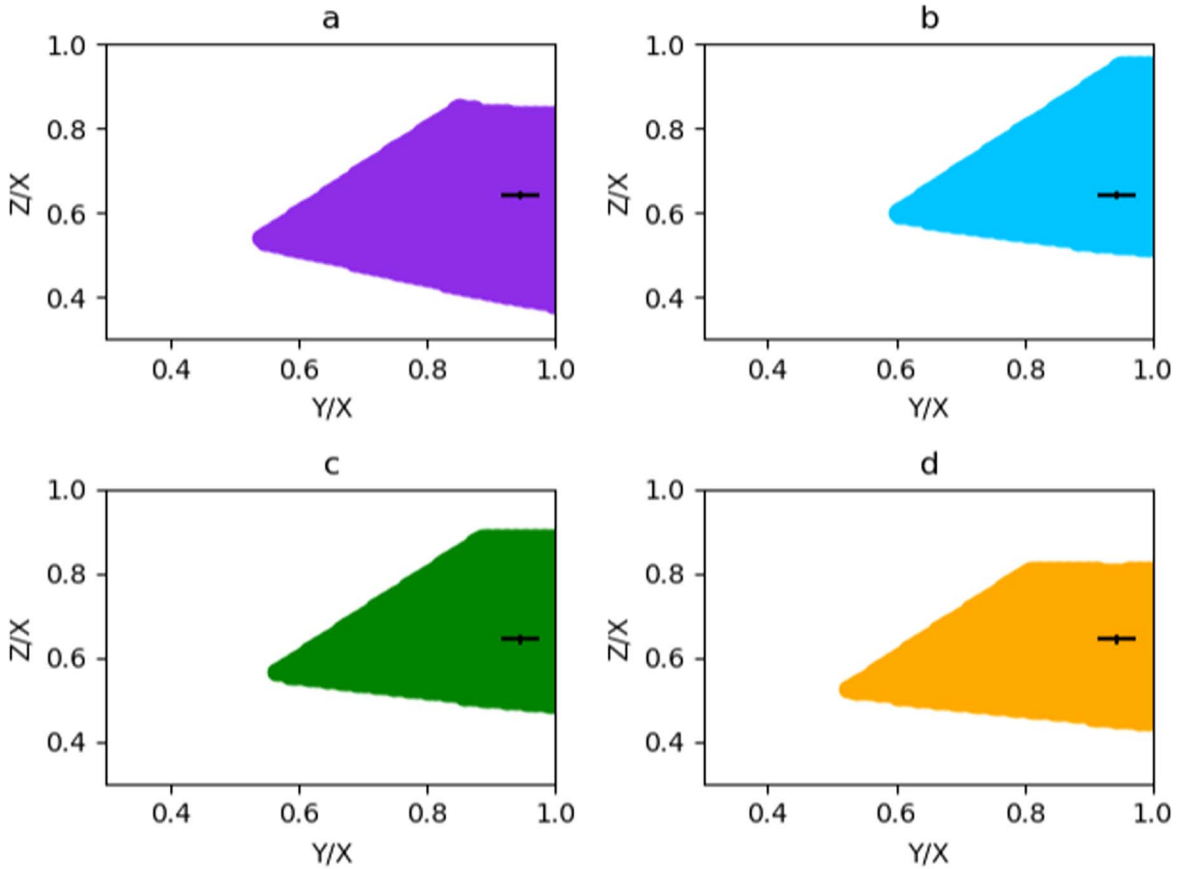


Figure 4. The $(p; q)$ plots showing the comparison between VADER results and DART Dimorphos shape (indicated, together with uncertainties, by the black cross): (a) image 4241; (b) image 4242; (c) image 4243; (d) image 4244.

Ratio” column of Table 2 for an incidence threshold at 100° , never compatible with 1 inside the errors.

This results in a total computed area of the ellipse projected in the LUKE FOV between 10,000 and 11,000 m^2 , with axis a (semimajor axis of the projected ellipse) in the range 66–69 m and axis b (semiminor axis of the projected ellipse) in the range 46–50 m (Table 2). Only the 4242 image seems to be slightly out of this range at a first guess; however, considering measurement errors, also the retrieved values for this image are consistent with the others.

To finally pass from the projected ellipse to the ellipsoid axis ratios, we used Equations (3a)–(3d). We only used the constraints defining oblate ellipsoids, i.e., $p < 1$ and $q < p$. The results have been then compared with the expected values for the Dimorphos ellipsoid axes computed using stereophotoclinometry applied to DRACO with the further support of LUKE data (Daly et al. 2024), i.e., $X = 179$ m, $Y = 169$ m, $Z = 115$ m, resulting in $p = 0.94 \pm 0.03$ and $q = 0.64 \pm 0.01$.

As shown in Figure 4, these ratios are well inside the range of variability of the analytical solution of Equations (3a)–(3d).

In addition, we also performed a sensitivity analysis considering illuminated pixels as those with an incidence angle larger than 90° , and, once more, results confirm that in this case we have to prefer the incidence angle threshold set at 100° (Figure 5).

In this case, the admitted regions in the $(p; q)$ plot include the Dimorphos shape as viewed by DART only as a very

borderline solution, thus further confirming the inadequate threshold value at 90° for the incidence angle for this study.

This demonstrates the feasibility of performing such an analysis, provided that the observational geometries are considered.

To consider the uncertainties related to the determination of the subspacescraft point, we also performed the same steps changing the predicted latitude and longitude values of $\pm 2^\circ$, obtaining results in line with those of the nominal case (see Figure 6).

The dayside hemisphere has not been analyzed in this work, primarily due to the presence of the plume that masks a variable part of the surface in images acquired both before and after the CA (Figure 7; Deshapriya et al. 2023; Dotto et al. 2024).

As the masking plume is evident in pre-CA images (Figure 7(a)), it is not straightforward to notice a similar effect in the post-CA images (Figure 7(b)).

However, even a very preliminary analysis shows that the plume casts a shadow over the dayside hemisphere of the asteroid (Deshapriya et al. 2023; Dotto et al. 2024) in post-CA images.

This is evidenced in Figure 7(c), where the ellipse computed by VADER for the 4241 image has been superimposed on the image at a short exposure time (i.e., 0.0007 s, with respect to the 0.035 s of the long exposure one used by VADER) belonging to the same triplet. In this image the ellipse centroid has been centered over the visible terminator.

Even if an accurate analysis is beyond the scope of the present work, this preliminary analysis helps in giving

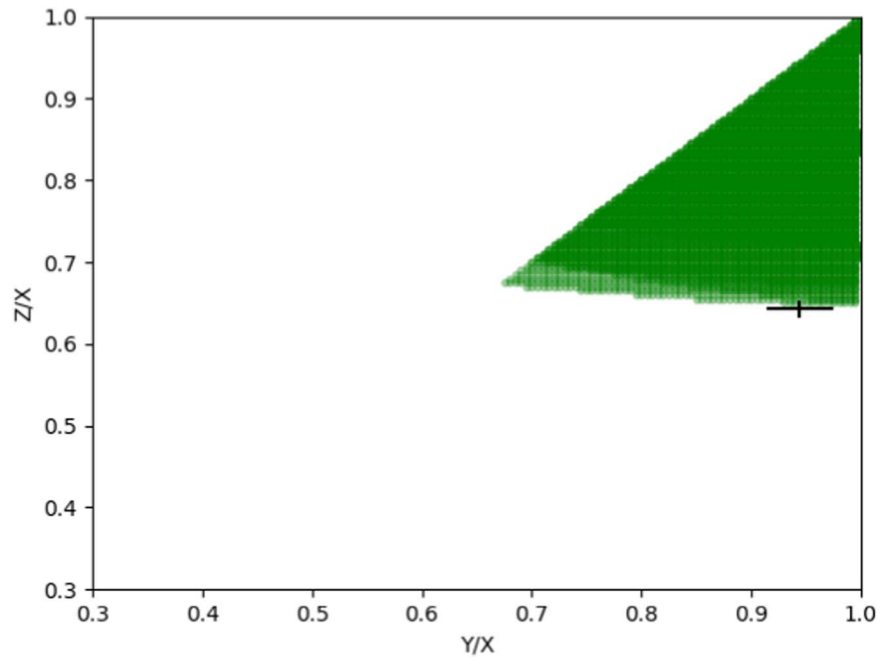


Figure 5. The $(p; q)$ plots for all the images taking into consideration the threshold for the incidence angle at 90° . The results of all the images are merged together: where the green is darker, more than one image has solutions. The black cross represents the DART Dimorphos shape with uncertainties.

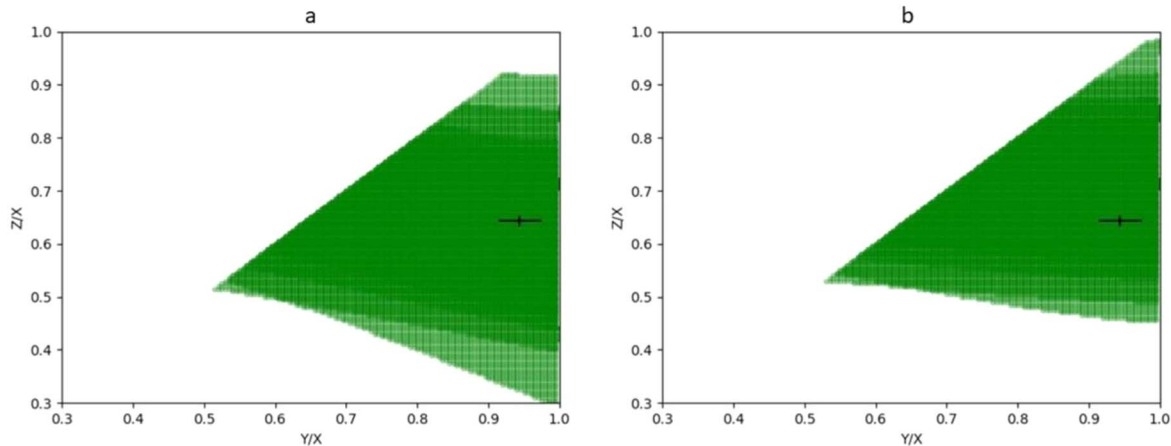


Figure 6. The $(p; q)$ plots for (a) the sub-S/C point changed by -2° in both latitude and longitude and (b) the sub-S/C point changed by $+2^\circ$ in both latitude and longitude. The results of all the images are merged together: where the green is darker, more than one image has solutions. The black cross represents the DART Dimorphos shape with uncertainties.

robustness to the findings described before. The ellipse retrieved using as input data from the nightside hemisphere seems to also fit well the shape for the dayside hemisphere if and only if the shadow by the plume (visible on the lower left side of the VADER ellipse) is accounted for.

5. Results

Daly et al. (2023, 2024) derived an oblate spheroid with X - and Y -axes very similar among them as the best match for the Dimorphos shape, using the DRACO DART high-resolution images, covering the full hemisphere during the pre-impact phase.

This reconstruction is based on the highest-resolution images of the target available up to now; however, this shape may be not usual among asteroids, particularly in secondaries of binary asteroid systems (Daly et al. 2023). While uncertainties are

high, observational statistics suggest that many binaries' secondaries tend to be elongated (Pravec et al. 2016). The reason that such an oblate secondary is rare or even unpreferred comes from the preference of elongation during the accumulation mechanisms under the gravity from the primary, where slow materials may approach the tidally locked, growing secondary along the radial direction. Such satellite configurations further evolve structurally due to the interactions with the primary at later stages (Sharma 2009, 2014).

For this reason, taking as input the results of the VADER algorithm, we included in our analysis all the shapes possible with oblate spheroids, as well as the ones predicted by theories and previous observations cited above and more elongated than the shape found by DART.

Indeed, as far as can be assessed by this work, the more elongated solution predicted by theories and expected on the

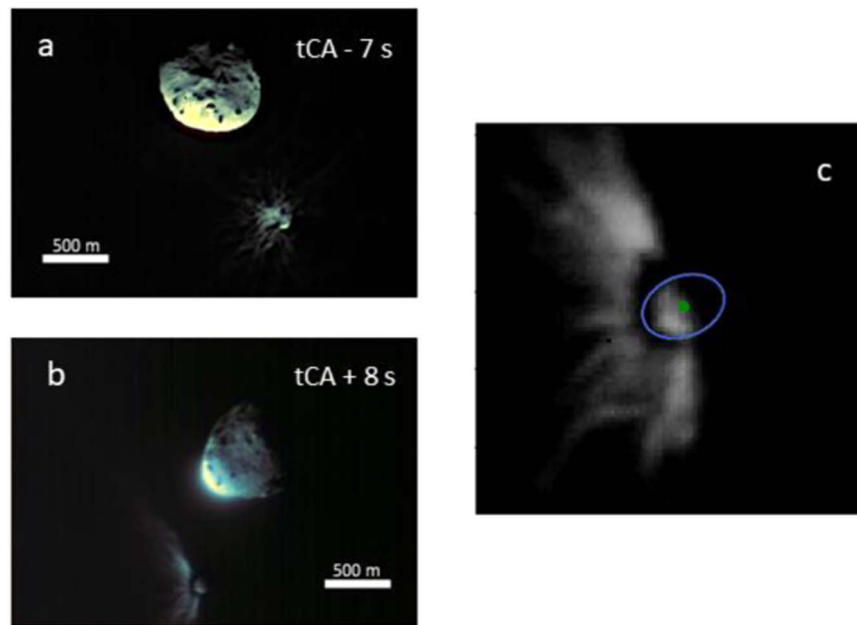


Figure 7. Zoom-in of images acquired by LUKE just (a) before and (b) after the CA, showing the plume partially covering the surface of Dimorphos. (c) Image `liciacube_luke_12_1664234241_00007_01` adequately zoomed in and contrasted, showing the plume shadow over the dayside hemisphere of Dimorphos. The shadow is visible on the lower left side of the ellipse. The green circle is the centroid of the blue ellipse, which is the same as that computed for the 4241 image with VADER.

basis of previous observations of other binary asteroid systems cannot be totally excluded in principle, as they are part of the allowed solutions (Figure 4).

On the other hand, the global shape model of Dimorphos, developed primarily using images from DART, is consistent with the constraints from LUKE images introduced here.

Reinforcing the need to use LUKE images to better assess the shape of Dimorphos toward a more elongated one is the comparison with the latest results obtained by means of stereophotoclinometry, including DART images with the support of LICIAcube images (Daly et al. 2024), shown in Table 3. Their results are an update of what was computed by Daly et al. (2023) and display a smaller ratio between Y - and X -axes, by using LUKE images to qualitatively assess the shape of Dimorphos.

For comparison, for this work we used p and q values where the probability density function (pdf) reaches its maximum value, taking into account all the solution points for the four LUKE images considered (as shown in Figure 4).

6. Conclusions

By using, for the first time ever, LICIAcube images to quantitatively constrain the shape of Dimorphos, we exploited the possibility, still not allowed by other instruments, of observing at disk-resolved resolutions a hemisphere of Dimorphos different from that impacted by DART.

Before obtaining higher spatial scale images with different viewing geometries owing to the Hera mission that will arrive at the Didymos–Dimorphos system (Michel et al. 2022), we can conclude that, with the given caveats and the small uncertainties of the DART observations, together with our methods used to infer the shape of Dimorphos from LUKE images, the shape derived in this work is consistent with that for Dimorphos found by using stereophotoclinometry (Daly et al. 2024).

Table 3

Comparison between the p and q Values for Dimorphos Found in This Work and in the Papers That Used DART DRACO Images

Source	p	q
This work	0.86 \pm 0.17	0.68 \pm 0.14
Daly et al. (2023)	0.98 \pm 0.02	0.66 \pm 0.01
Daly et al. (2024)	0.94 \pm 0.03	0.64 \pm 0.01

Note. The values for this work are computed as the solutions of Equations (3a)–(3d), where the pdf reaches its maximum and 20% has been used for the error.

However, the availability of LICIAcube data, looking at an unexplored area of Dimorphos, has opened the possibility to a more elongated shape for the asteroid ellipsoid, not limited to the measurement errors assessed by DRACO and making it more similar to what has been retrieved for the majority of the secondaries observed so far and what is expected by the theoretical considerations (Pravec et al. 2016; Sharma 2009, 2014).

It is worth mentioning that the accuracy of such an analysis would be hard to match without the development and usage of the VADER algorithm. Thanks to its semiautomatic capabilities, it helped in robustly delineating the shape of the nighttime Dimorphos hemisphere viewed by LUKE, as well as providing quantitative measurement of the parameters needed as input in this work.

Finally, we note that VADER, as a stand-alone CV algorithm, is not devoted only to the LUKE images and can be used in the future for studies implying image analysis at large.















Acknowledgments






This work was supported by the Italian Space Agency (ASI) within the LICIAcube project (ASI-INAF agreement AC No. 2019-31-HH.0) and by the DART mission, NASA contract 80MSFC20D0004.

Data Availability

The Dimorphos viewing geometry presented here was computed using data files available at <https://naif.jpl.nasa.gov/naif/data.html>. The LICIACube data set is published on the PDS Small Bodies Node (https://pds-smallbodies.astro.umd.edu/data_sb/missions/dart/index.shtml) and is also available at the LICIACube SOC (<https://www.ssd.csi.it/liciacube/>), where all the relevant SPICE kernels are also stored.

ORCID iDs

Angelo Zinzi  <https://orcid.org/0000-0001-5263-5348>
 P. H. A. Hasselmann  <https://orcid.org/0000-0003-1193-8945>
 A. Lucchetti  <https://orcid.org/0000-0001-7413-3058>
 M. Pajola  <https://orcid.org/0000-0002-3144-1277>
 A. Rossi  <https://orcid.org/0000-0001-9311-2869>
 R. T. Daly  <https://orcid.org/0000-0002-1320-2985>
 M. Hirabayashi  <https://orcid.org/0000-0002-1821-5689>
 T. Farnham  <https://orcid.org/0000-0002-4767-9861>
 C. M. Ernst  <https://orcid.org/0000-0002-9434-7886>
 S. L. Ivanovski  <https://orcid.org/0000-0002-8068-7695>
 J.-Y. Li  <https://orcid.org/0000-0003-3841-9977>
 M. Amoroso  <https://orcid.org/0000-0003-2603-165X>
 J. R. Brucato  <https://orcid.org/0000-0002-4738-5521>
 E. Gramigna  <https://orcid.org/0000-0001-8776-7922>

S. Ieva  <https://orcid.org/0000-0001-8694-9038>
 R. Lasagni Manghi  <https://orcid.org/0000-0002-5733-2554>
 D. Perna  <https://orcid.org/0000-0002-4545-3850>
 G. Poggiali  <https://orcid.org/0000-0002-3239-1697>
 P. Tortora  <https://orcid.org/0000-0001-9259-7673>

References

- Acton, C. H. 1996, *P&SS*, 44, 65
 Acton, C., Bachman, N., Semenov, B., & Wright, E. 2017, *P&SS*, 150, 9
 Binggeli, B. 1980, *A&A*, 82, 289
 Carlsson, K. 2016, *Imaging Physics* (Stockholm: KTH Applied Physics), <https://www.kth.se/social/files/57d11da0f276542d9216413a/Comp.ImagingPhysics.new.pdf>
 Daly, R. T., Ernst, C. M., Barnouin, O. S., et al. 2023, *Natur*, 616, 443
 Daly, R. T., Ernst, C. M., Barnouin, O. S., et al. 2024, *PSJ*, 5, 24
 Deshapriya, J. D. P., Hasselmann, P. H., Gai, I., et al. 2023, *PSJ*, 4, 231
 Dotto, E., & Zinzi, A. 2023, *NatCo*, 14, 3055
 Dotto, E., Della Corte, V., Amoroso, M., et al. 2021, *P&SS*, 199, 105185
 Dotto, E., Deshapriya, J. D. P., Gai, I., et al. 2024, *Natur*, 627, 505
 Fletcher, Z. J., Ryan, K. J., Ernst, C. M., et al. 2022, *Proc. SPIE*, 12180, 121800E
 Menon, D., Andriani, S., & Calvagno, G. 2007, *ITIP*, 16, 132
 Michel, P., Kuppers, M., Campo Bagatin, A., et al. 2022, *PSJ*, 3, 160
 Pravec, P., Scheirich, P., Kušnirák, P., et al. 2016, *Icar*, 267, 267
 Rivkin, A. S., Chabot, N. L., Stickle, A. M., et al. 2021, *PSJ*, 2, 173
 Sharma, I. 2009, *Icar*, 200, 636
 Sharma, I. 2014, *Icar*, 229, 278
 Thomas, C. A., Naidu, S. P., Scheirich, P., et al. 2023, *Natur*, 616, 448